Supporting Information

Porphyrin Nanoribbon Based Spin Filtering Device

Gargee Bhattacharyya,[†] Rameshwar L. Kumawat,[†] Biswarup Pathak, [†,#,*]

[†]Discipline of Metallurgy Engineering and Materials Science, [#]Discipline of Chemistry, School of Basic Sciences and, Indian Institute of Technology (IIT) Indore, Indore, Madhya Pradesh, 453552, India
Email: biswarup@iiti.ac.in

Contents:

Figure S6: Spin density distribution of (a) $(B-B)_a^H - PA$, (b) $(B-B)_a^F - PA$, (c) $(B-B)_b^H - PA$ and (d) $(B-B)_b^F - PA$ systems.

Figure S7: Optimized structures and spin polarized density of states of (a) B doped, (b) Al doped, and (c) two B doped C=C embedded porphyrin monolayer systems.

Text S2: Energetic stability and experimental realization

Table S1: Formation energies per dopant (E_F), magnetic moments per dopant (μB), nature of the system and spin gap (eV) for the B and Al doped C=C embedded PA. Here M, SHM, WHM, and S denote metallic, strong half-metallic, weak half-metallic, and semiconducting, respectively.

Text S3: Dynamic and thermal stability

Figure S8: (a) Optimized structures, (b) phonon dispersion plot and (c) total energy fluctuation of AIMD simulations of $B@(C=C)_a^F - PA$ system. Displacement eigenvectors (indicated by blue arrows) corresponding to the soft phonon mode with imaginary frequencies of (d) 0.15 cm^{-1}, (e) 1.29 cm^{-1} and (f) 30.72 cm^{-1} of $B@(C=C)_a^F - PA$ system.

Figure S9: Optimized structure and phonon dispersion plot of $(C=C)_a^F - PA$ system.

Table S2: Bader charge analysis of pure $(C=C)_a^F - PA$ and B doped $B@(C=C)_a^F - PA$.

Text S4: Calculation of Magnetic anisotropy energy (MAE)

Table S3: Summary of magnetic anisotropy energies in μeV/vacancy and the easy axis for $B@(C=C)_a^F - PA$.

Table S4: Modulation of spin-up gap (eV) in and nature of the $B@(C=C)_a^F - PA$ system with % of applied strain along uniaxial-tensile and uniaxial-compressive direction.

Figure S10: (a)-(e) Optimized structure, spin density distribution and TDOS plot of $B@(C=C)_a^F - PA$ under the application of uniaxial tensile strain from 1% to 5%.

Figure S11: (a)-(e) Optimized structure, spin density distribution and TDOS plot of $B@(C=C)_a^F - PA$ under the application of uniaxial compressive strain from 1% to 5%.

Text S1: **Computational Details**

Formation Energy Calculation:

Energetic stabilities of B/Al doped H/F-terminated C=C embedded porphyrin nanoribbon have been investigated from formation energy (E_F) calculation. The formation energy[1] is calculated using the following equation:

$$E_F = \left(E_{B/Al@Porphyrin-NR} - E_{Porphyrin-NR}\right) - \left(\mu_{B/Al(Bulk)} - \mu_{C(Bulk)}\right) \quad (1)$$

Where $E_{B/Al@Porphyrin-NR}$ is the total energy of B/Al doped C=C embedded porphyrin nanoribbon, $E_{Porphyrin-NR}$ is the total energy of pure C=C embedded porphyrin nanoribbon, $\mu_{B/Al(Bulk)}$ is the chemical potential of B/Al atom from its bulk from α-rhombohedral boron/aluminium bulk BCC structure[2-3] and $\mu_{C(Bulk)}$ is the chemical potential of C atom from graphene structure.[4]

Magnetic anisotropic energy (MAE) and Spin density difference (SDD):

Magnetic anisotropic energy (MAE)[5] is also calculated for our best system B doped C=C embedded porphyrin nanoribbon unit, i.e. $B@(C=C)_a^F - PA$ system to investigate the thermal stability of spin fluctuation upon external thermal energy. MAE[6] per unitcell is calculated including spin-orbit coupling (SOC) effect using the equation described below where E_{EA} is the energy of the system along easy axis when an external magnetic field is applied and E_{HA} is the energy of the system along hard axis under application of magnetic field. We have considered our calculation along magnetizing direction (100), (010), (110), (111) and (001).

$$MAE = E_{HA} - E_{EA} \quad (2)$$

Additionally, to comprehend the nature of electron spin density in B doped C=C embedded porphyrin monolayer; the spin density distribution (SDD)[7] is plotted. The SDD is calculated using the following equation

$$\rho_{SD} = \rho_{up} - \rho_{down} \quad (3)$$

Here, the up and down electron spin density are denoted as ρ_{up} and ρ_{down}, respectively. In the SDD, the up spin density of wave functions for different lobes are indicated by yellow colors and the down spin density of wave functions for different lobes are indicated by blue colors. The direct mapping of the electron spin density is measured experimentally by the neutron diffraction in electron spin resonance (ESR) spectroscopy.[8]

Dynamic and Thermal Stability:

Dynamic stability of our proposed system $B@(C=C)_a^F - PA$ is investigated from phonon frequency and phonon dispersion calculations. The phonon frequency calculations were performed using the density functional perturbation theory (DFPT)[9] as implemented in VASP, and phonon dispersion calculations were carried out using Phonopy code.[10]

Furthermore, thermal stability of $B@(C=C)_a^F - PA$ system was verified by carrying out ab initio molecular dynamics simulations (AIMD) using a canonical ensemble at 300 K with a time step of 1 fs for 20 ps. The Nose´ thermostat model was used to control the temperature throughout the MD simulations.[11]

Computational Details for Transport Studies of Spin Filtering Devices

We have used gold (Au (111)) nanowires as electrodes and central scattering region. After relaxation, thiol (-SH) groups are deprotonated and covalently connected to gold (Au) contact in the "atop" position. The Au-S bond distances are fixed at ~2.32 Å, and the Au contacts are modelled according to the Au nano-contact geometry.[12] Here, the gold electrode does not enclose the porphyrin molecule as the gold electrodes are defined as 1D nanoelectrodes. We have used here the optimized structures of pure [$(C=C)_a^F - PA_n\,(n=1)$] and B doped C=C embedded porphyrin [$B@(C=C)_a^F - PA_n\,(n=1,\ 2)$] with edges terminated with fluorine (F) as our scattering region. Each Au unit cell has two sublayers of either three or seven Au atoms with periodic boundary conditions along the $z-$ direction (transport direction). An extra seven-atom layer is inserted between the right electrode and the molecule to ensure the same attachment of the molecule to the left and right electrodes. We have used here the optimized structures of pure [$(C=C)_a^F - PA_n\,(n=1)$] and B doped C=C embedded porphyrin [$B@(C=C)_a^F - PA_n\,(n=1,\ 2)$] with edges terminated with fluorine (F) to model the metal-molecule-metal nanoscale devices.

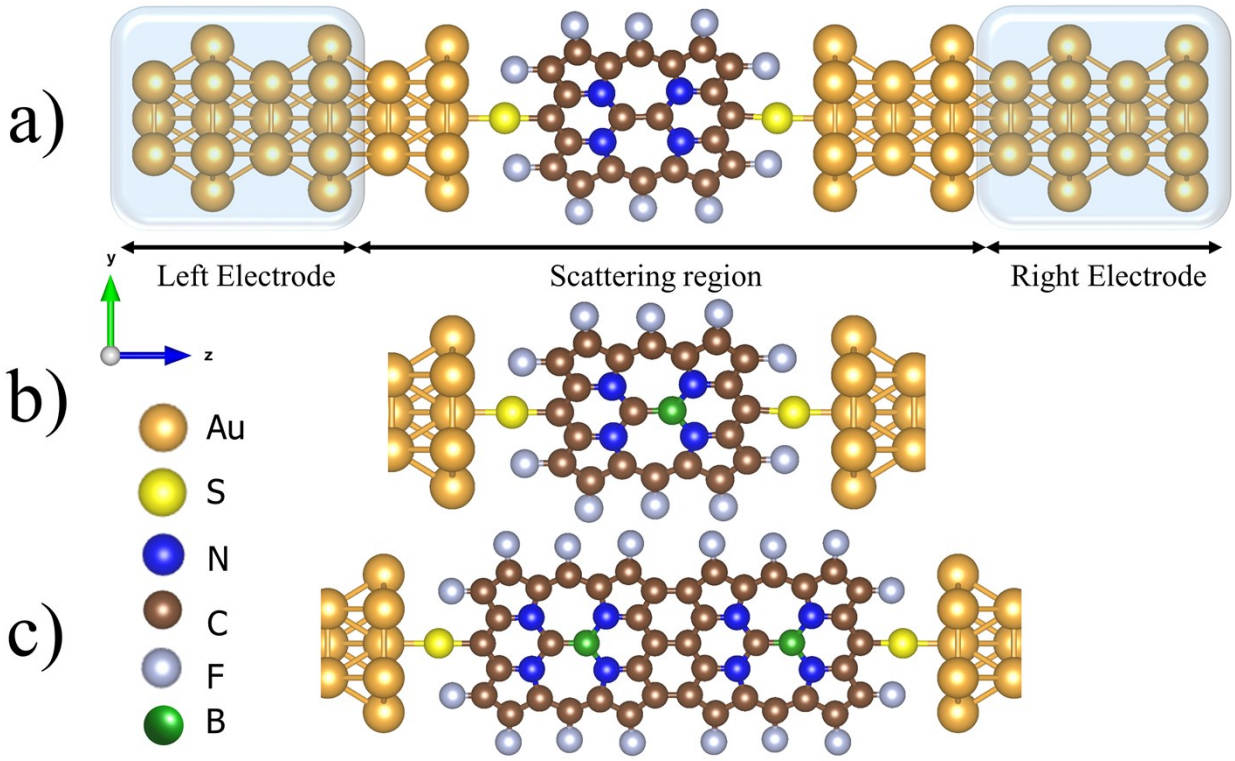

Figure S1: Schematic illustration of the proposed molecular nanoscale devices containing: (a) $[(C=C)_a^F - PA_n\,(n=1)]$, (b) $[B@(C=C)_a^F - PA_n\,(n=1)]$, and (c) $[B@(C=C)_a^F - PA_n\,(n=2)]$ units.

The proposed system is divided into three parts: left (L), right (R), and a central scattering region as shown in Figure S1. Transport properties are computed by using the extended three-system model (Figure S1). First principles DFT calculations are performed employing the SIESTA (Spanish Initiative for Electronic Simulations with Thousands of Atoms) code[13] within the generalized gradient approbation (GGA) with the Perdew, Burke, and Ernzerhof (PBE) functional for geometrical relaxation.[14] Norm-conserved Troullier-Martins pseudopotentials[15] are employed to describe the interaction between the core and valence electrons. The energy cut off for the real space grid is 150 Ry. To sample the Brillouin zone integration, we employed the gamma point sampling for the extended molecular region and a 1 × 1 × 50 within the Monkhorst-Pack scheme for electrodes with a double-ζ polarized basis set. The

systems are fully relaxed by employing the conjugate gradient (CG) algorithm. The tolerance in density matrix difference is 0.0001 and the residual forces on the atoms are less than 0.01 eV/Å. The transmission function and $I-V$ characteristics curves are computed by combining the non-equilibrium Green's function (NEGF) and DFT approach, as implemented in TranSIESTA module of SIESTA code.[13] The transmission function, which defines the possibility of an electron to be transmitted from left electrode to right electrode through the central scattering region with specific energy (E), has been calculated form the given equation:[13,16]

$$T(E,V) = tr[\Gamma_R(E,V)G_C(E,V)\Gamma_L(E,V){G_c}^{\dagger}(E,V)] \quad (4)$$

Where G_C is the Green's function of the central scattering region and is the coupling matrix of L/R electrodes. Further, the integration of transmission function provides the electric current as by given equation:[13, 16]

$$I(V_b) = \frac{2e}{h}\int_{\mu_R}^{\mu_L} T(E,V_b)\left[f(E-\mu_L) - f(E-\mu_R)\right]dE \quad (5)$$

Where $T(E,V_b)$ is to represent the transmission spectrum of the electrons entering at energy (E) from L to R electrode in presence of an applied finite bias voltage V_b, $f(E-\mu_{L,R})$ is showing the Fermi-Dirac distribution of electrons in the L and R electrodes and $\mu_{L,R}$ the chemical potential where $\mu_{L/R} = E_F \pm V_b/2$ are moved correspondingly up and down according to the Fermi energy E_F.[13, 16]

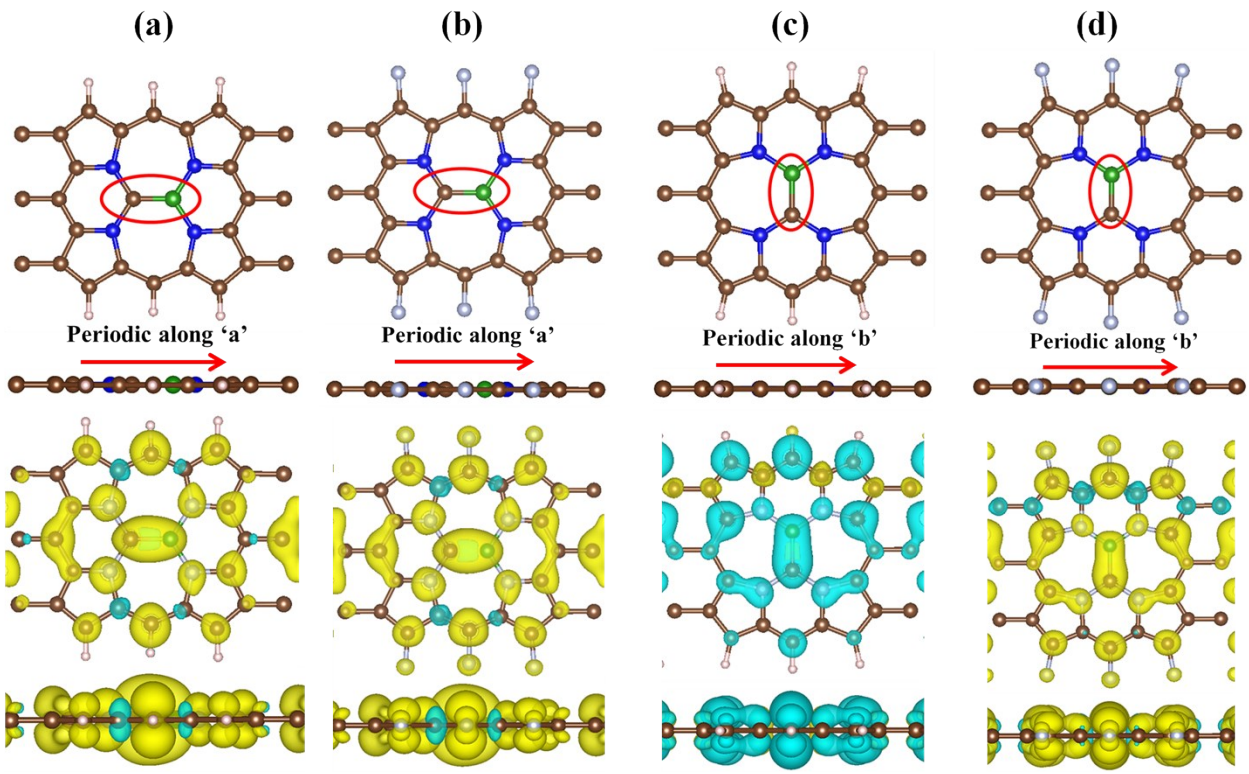

Figure S2: Spin density distribution of (a) $B@(C=C)_a^H - PA$, (b) $B@(C=C)_a^F - PA$, (c) $B@(C=C)_b^H - PA$ and (d) $B@(C=C)_b^F - PA$ systems.

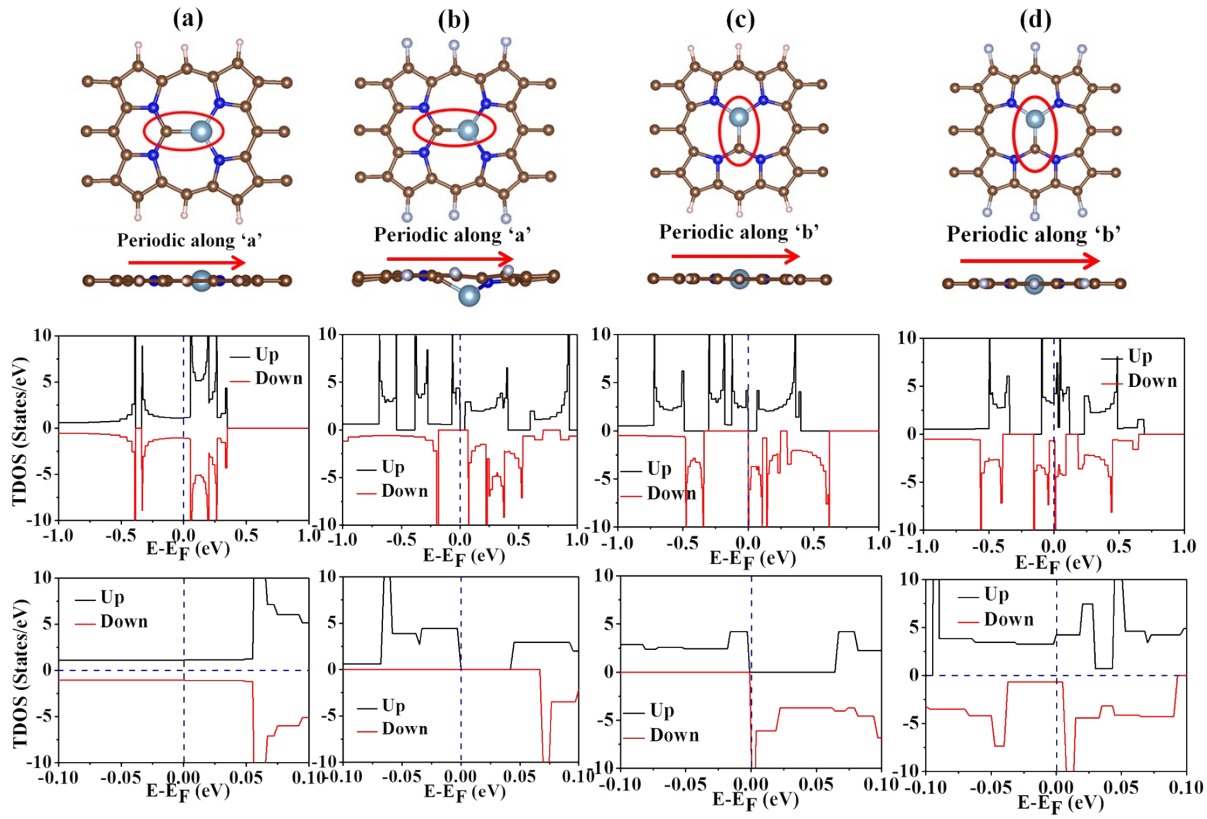

Figure S3: Optimized structures, spin polarized density of states and magnified spin polarized density of states (third panel) of (a) $Al@(C=C)_a^H - PA$, (b) $Al@(C=C)_a^F - PA$, (c) $Al@(C=C)_b^H - PA$ and (d) $Al@(C=C)_b^F - PA$ systems. The Fermi level is set to zero and is indicated by a blue dashed line. The Al, C, N, H and F atoms are denoted by sky blue, brown, blue, white and light gray colors.

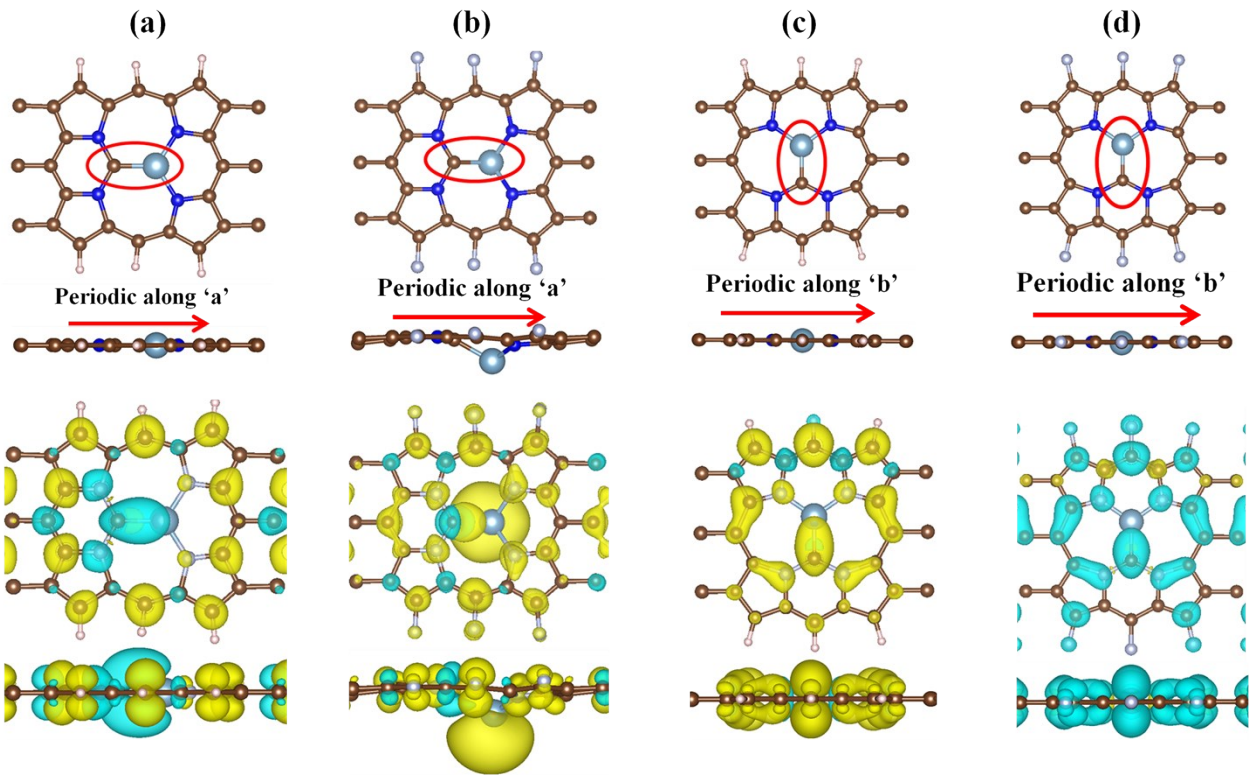

Figure S4: Spin density distribution of (a) $Al@(C=C)_a^H - PA$, (b) $Al@(C=C)_a^F - PA$, (c) $Al@(C=C)_b^H - PA$ and (d) $Al@(C=C)_b^F - PA$ systems.

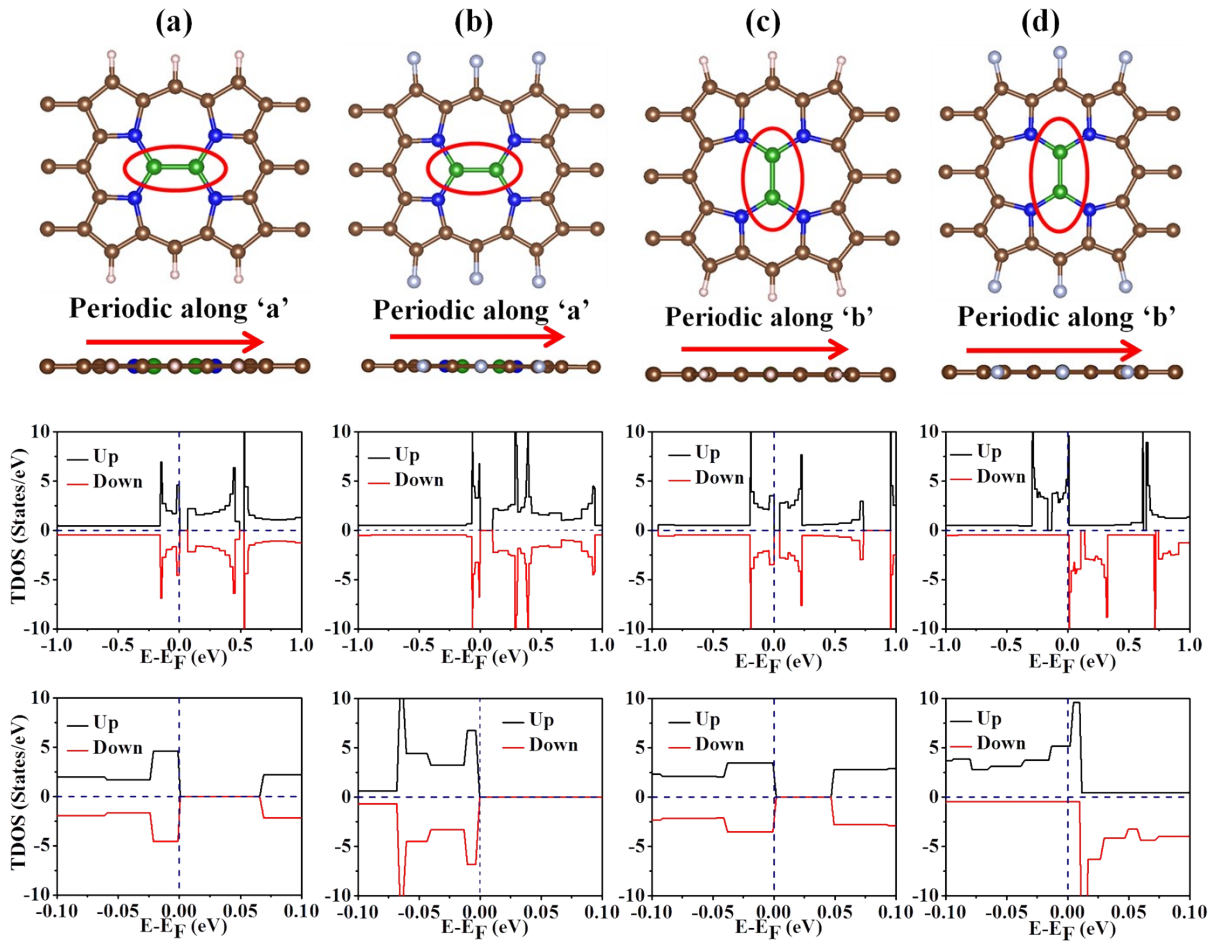

Figure S5: Optimized structures, spin polarized density of states and magnified spin polarized density of states (third panel) of (a) $(B-B)_a^H - PA$, (b) $(B-B)_a^F - PA$, (c) $(B-B)_b^H - PA$ and (d) $(B-B)_b^F - PA$ systems. The Fermi level is set to zero and is indicated by a blue dashed line. The B, C, N, H and F atoms are denoted by green, brown, blue, white and light gray colors.

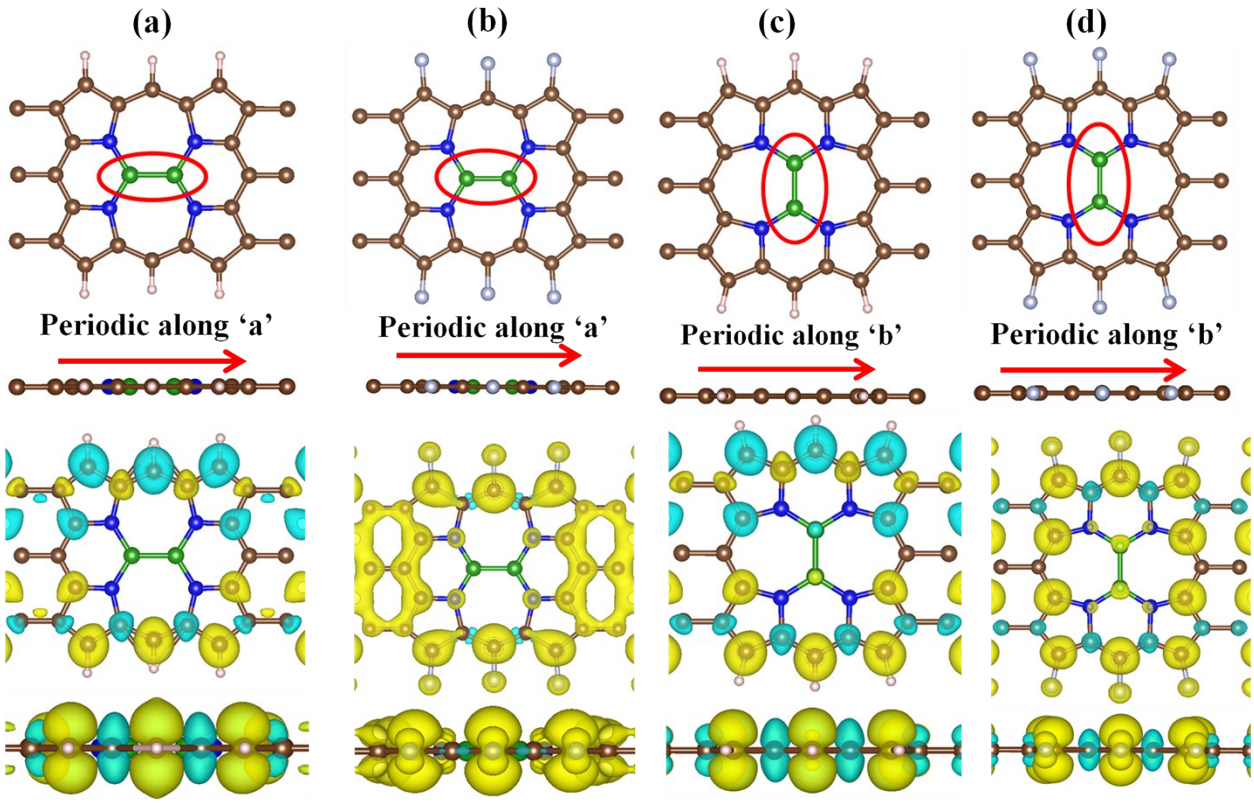

Figure S6: Spin density distribution of (a) $(B-B)_a^H - PA$, (b) $(B-B)_a^F - PA$, (c) $(B-B)_b^H - PA$ and (d) $(B-B)_b^F - PA$ systems.

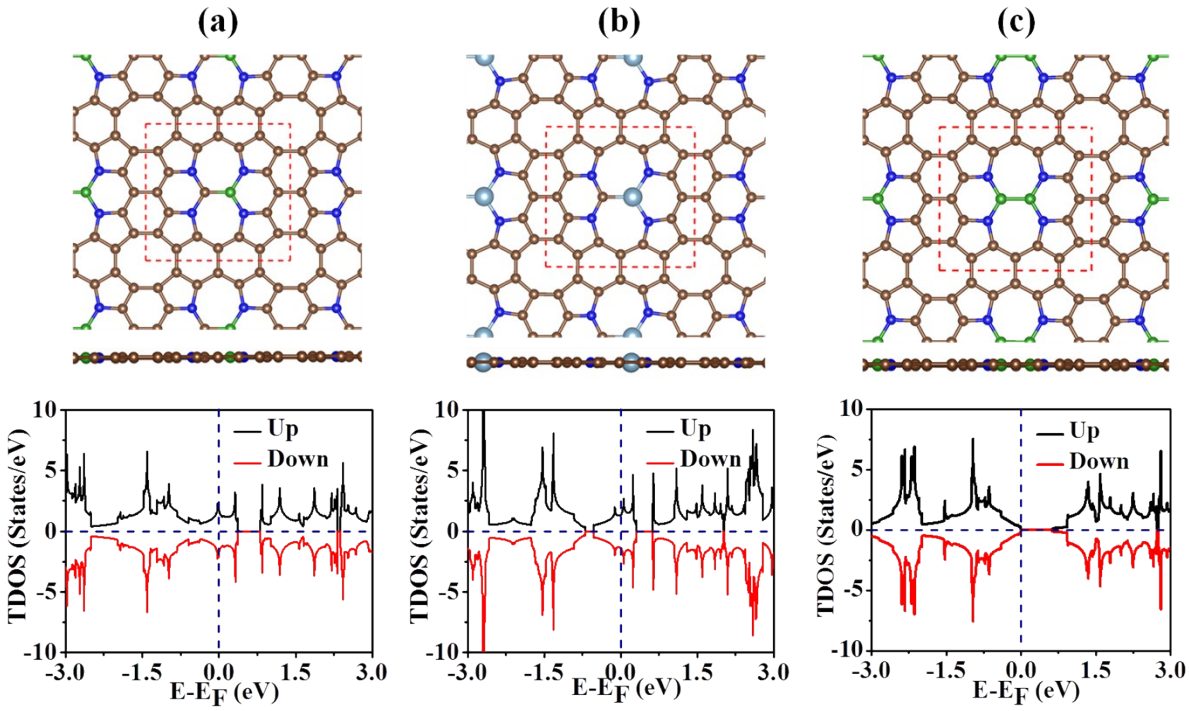

Figure S7: Optimized structures and spin polarized density of states of (a) B doped, (b) Al doped, and (c) two B doped C=C embedded porphyrin monolayer systems (unit cell is shown in the red dotted line).

Text S2: Energetic stability and experimental realization

Our stability analysis of the nanostructures begins with energetic stability analysis. To evaluate the stability of these systems we have calculated formation energy of these doped systems [Text S1, Supporting Information]. The formation energy values of B and Al-doped systems are given in Table S1. It has been found that the formation energies of the B-doped nanoribbon systems are negative. A negative value of formation energies indicates that formations of B-doped nanoribbons are experimentally feasible. On the other hand, formation of Al-doped systems is not favourable. Similar negative values have been reported for B-doped C_3N monolayer system (-1.54 eV/atom), where C has been replaced by B atom.[17] Moreover; the possibility of B-doping in C-matrix has also been discussed in earlier experimental reports.[17-18] Among all the

B doped arrays, $B@(C=C)_a^F - PA$ has half-metallic character and formation energy of -2.59 eV/atom. Therefore we can also conclude the possibility of realization of our proposed $B@(C=C)_a^F - PA$ structure.

Table S1: Formation energies per dopant (E_F), magnetic moments per dopant (μB), nature of the system and spin gap (eV) for the B and Al doped C=C embedded PA. Here M, SHM, WHM, and S denote metallic, strong half-metallic, weak half-metallic, and semiconducting, respectively.

System	E_F (eV/atom)	Magnetic moment (μB)	Nature	Spin Gap (eV)
$B@(C=C)_a^H - PA$	-2.50	0.4126	M	0
$B@(C=C)_a^F - PA$	-2.59	1.0000	SHM	0.37
$B@(C=C)_b^H - PA$	-2.84	1.0000	WHM	0.21
$B@(C=C)_b^F - PA$	-2.97	1.0000	S	-
$Al@(C=C)_a^H - PA$	3.11	0.0085	M	0
$Al@(C=C)_a^F - PA$	2.82	1.0000	S	-
$Al@(C=C)_b^H - PA$	3.05	1.0000	WHM	0.06
$Al@(C=C)_b^F - PA$	2.92	0.2077	S	-

Elemental boron (B) and nitrogen (N) have already been attracted researcher's attention as dopant for graphene due to their similar atomic radii like carbon (C).[17] Boron doped graphene has been also synthesized by several research groups using different approaches.[17] Most widely used method for the synthesis of B doped graphene is solid state reaction between graphite powder or GO and a boron precursor mainly H_3BO_3, B_2O_3 or B_4C and subsequently exfoliation of single B-G sheets.[19-20] B doped graphene nanoribbons have also been synthesized experimentally by Kawai *et al.*[21] and Xing *et al.*[22] using a separate method. Moreover, it is also mentioned that porphyrin complexes with smaller atoms (like boron (B) and carbon-carbon (C=C)) bonded to nitrogen (N) have been synthesized.[23] In recent past, Brothers *et al.* also explored experimental synthesization of boron porphyrin complexes.[24]

Therefore, we believe that B doped C=C embedded porphyrin nanoribbon may be synthesized in the near future.

Text S3: Dynamic and thermal stability

We have analyzed dynamic and thermal stability of $B@(C=C)_a^F-PA$ through phonon dispersion calculations (Figure S8a-b) and *ab initio* molecular dynamics (AIMD) simulation (Figure S8c), respectively. Phonon dispersion calculation of $B@(C=C)_a^F-PA$ reveals that our system has small imaginary frequencies. To be precise, there are three imaginary frequencies with the values of 0.15, 1.29 and 30.72 cm^{-1} respectively. Analysis of phonon frequency discloses that these imaginary modes do not originate from any non-trivial motion[25] of atoms against each other rather the first two modes (0.15, 1.29 cm^{-1}) originate from pure translational motion and the third mode (30.72 cm^{-1}) originates from bending motions of a group of atoms (Figure S8d-f). Moreover, we have found that undoped fluorinated array also exhibits slight imaginary frequencies (4.00 cm^{-1}) in its phonon dispersion plot (Figure S9). Therefore, it can be stated that our system $B@(C=C)_a^F-PA$ may be stabilized after connecting to electrodes while making spin-filtering device.

Thermal stability of $B@(C=C)_a^F-PA$ is analyzed by *ab initio* molecular dynamics (AIMD) simulation using an NVT ensemble at 300 K with a time step of 1 fs (femtosecond) for 20 ps (picoseconds). Room temperature AIMD simulation does not show any possibility of inter-conversion of the optimized structure (Figure S8c). Thus, it can be stated that our system $B@(C=C)_a^F-PA$ is thermally stable.

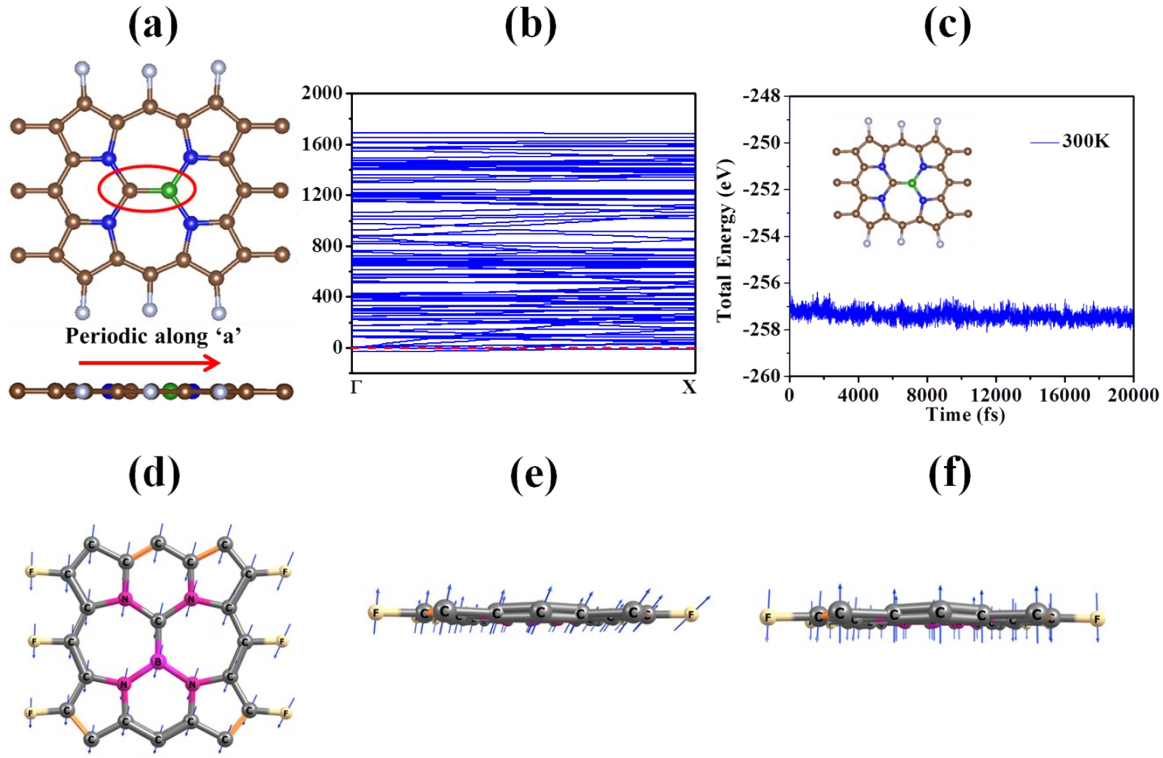

Figure S8: (a) Optimized structures, (b) phonon dispersion plot and (c) total energy fluctuation of AIMD simulations of $B@(C=C)_a^F - PA$ system. Displacement eigenvectors (indicated by blue arrows) corresponding to the soft phonon mode with imaginary frequencies of (d) 0.15 cm^{-1}, (e) 1.29 cm^{-1} and (f) 30.72 cm^{-1} of $B@(C=C)_a^F - PA$ system.

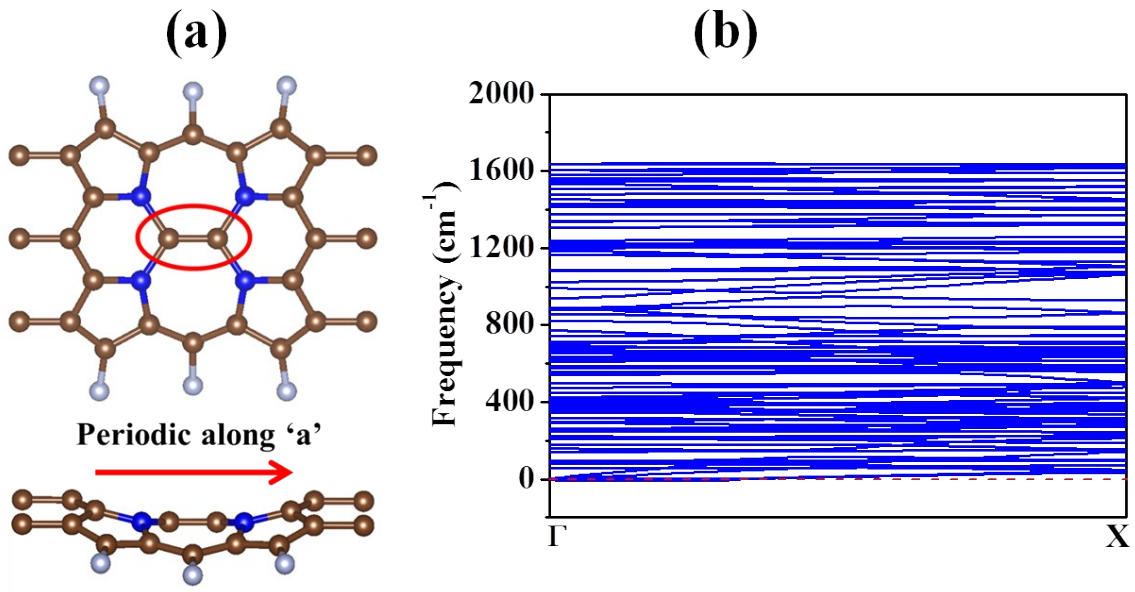

Figure S9: Optimized structure and phonon dispersion plot of $(C=C)_a^F - PA$ system.

Table S2: Bader charge analysis of pure $(C=C)_a^F - PA$ and B doped $B@(C=C)_a^F - PA$.

Net Effective Charge in System $(C=C)_a^F - PA$	**Net Effective Charge in System** $B@(C=C)_a^F - PA$
C_{12}=+0.6888|e|, N_1=-1.1692|e|, N_4=-1.1836|e|	C_{11}=-0.1022|e|, N_1=-1.4814|e|, N_4=-1.4729|e|

Text S4: Calculation of Magnetic Anisotropy Energy (MAE)

The magnetic anisotropy energy (MAE) is calculated by applying the torque approach.[26-27] Non-collinear self-consistent calculations (including spin orbit coupling) are performed in the <001>, <010>, <100>, <110> and <111> axis magnetization directions, respectively. MAE originates from the perpendicular and in plane contribution of spin orbit coupling (SOC), which can be expressed in terms of angular momentum operators L_X, L_Y *or* L_Z. So the contribution of different spins can be expressed by the second order perturbation equation.[28]

$$MAE = \xi^2 \sum_{0,u} \frac{| < o|L_z|u > |^2 - | < o|L_x|u > |^2}{E_u - E_o} \qquad (6)$$

Here, o and u represent the occupied and unoccupied electronic states, respectively. The E_o and E_u in the denominator are their respective band energies. L_Z and L_X are the angular momentum operators along Z and X axis, and ξ denotes the strength of the SOC. So, a potential with good MAE for practical application should hold a high value of ξ.

Table S3: Summary of magnetic anisotropy energies in μeV/vacancy and the easy axis for $B@(C=C)_a^F$ - PA system.

$B@(C=C)_a^F - PA$	**Easy Axis (100)**	**(001)-(100)**	**(010)-(100)**	**(110)-(100)**	**(111)-(100)**
	0	0.04 μeV	0.03 μeV	**0.05 μeV**	0.02 μeV

Text S5: Effect of strain on half-metallicity in $B@(C=C)_a^F - PA$

It is also very vital to analyze the effect of strain on magnetism and half-metallic properties on $B@(C=C)_a^F - PA$ for its practical application. Therefore, we have applied both uniaxial tensile and compressive strain ranging from 1% to 5% to scrutinize the nature of the system and the modulation of the spin-up gap in $B@(C=C)_a^F - PA$ system. It has been observed that our system only holds its half-metallic characteristics under 2% and 3% uniaxial tensile strain. Under uniaxial compressive strain, our system became semiconducting at lower % of strain (1% - 2%), and then we observe a semiconducting to metallic phase transition which continues up to 5% applied strain. Spin gap of half-metallic systems has been tabulated in Table S4. We have also included the optimized structure, spin density distribution and TDOS plot under the application of strain from 1% to 5% in Figure S10-S11.

Table S4: Modulation of spin-up gap (eV) in and nature of the $B@(C=C)_a^F - PA$ system with % of applied strain along uniaxial-tensile and uniaxial-compressive direction.

% of applied Strain	**Uniaxial-tensile**		**Uniaxial-compressive**	
	Spin-Up Gap (eV)	**Nature of the system**	**Spin-Up Gap (eV)**	**Nature of the system**
1%	-	S	-	S
2%	0.355	HM	-	S
3%	0.347	HM	-	M
4%	-	S	-	M
5%	-	S	-	M

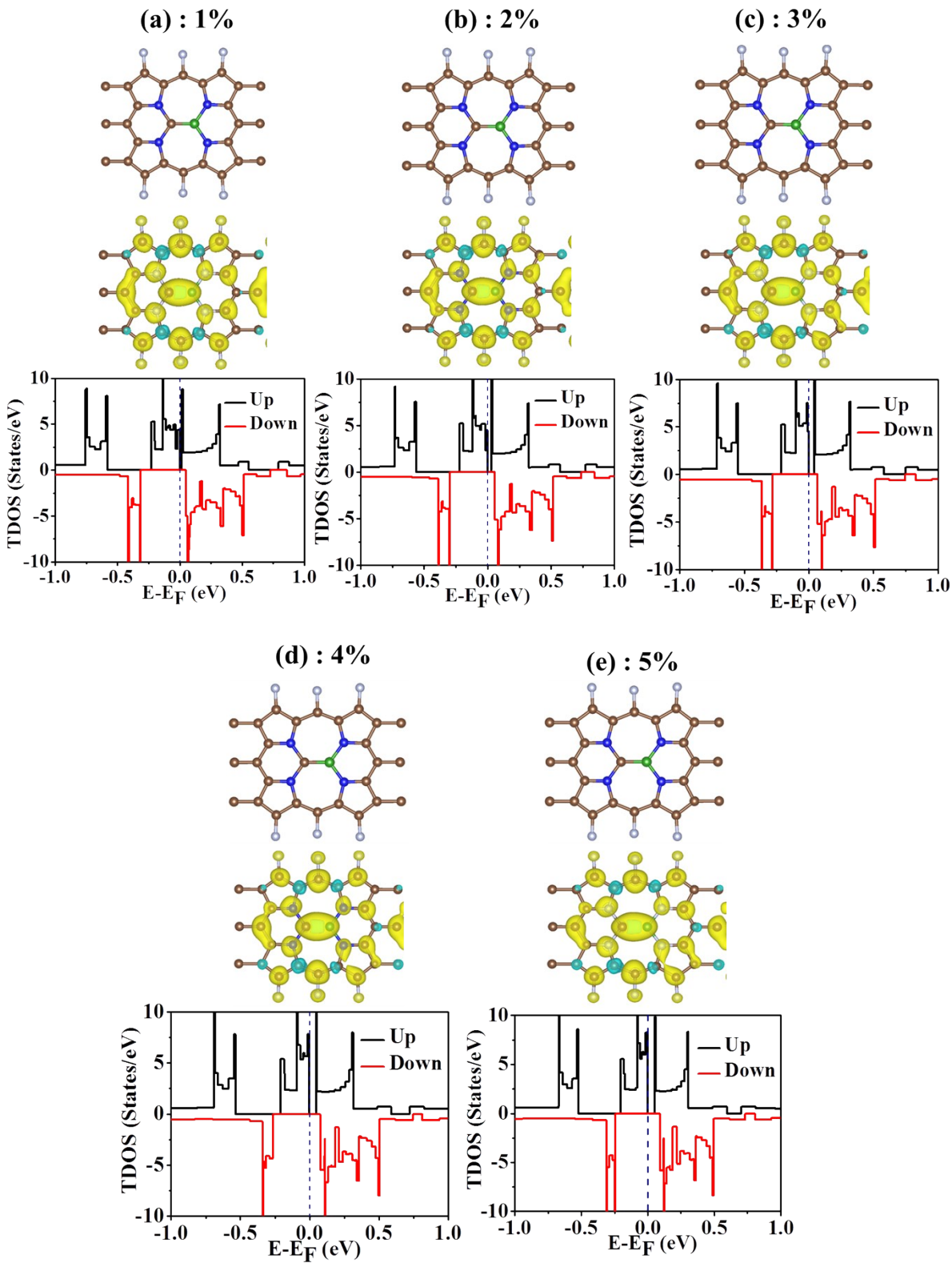

Figure S10: (a)-(e) Optimized structure, spin density distribution and TDOS plot of $B@(C=C)_a^F - PA$ under the application of uniaxial tensile strain from 1% to 5%.

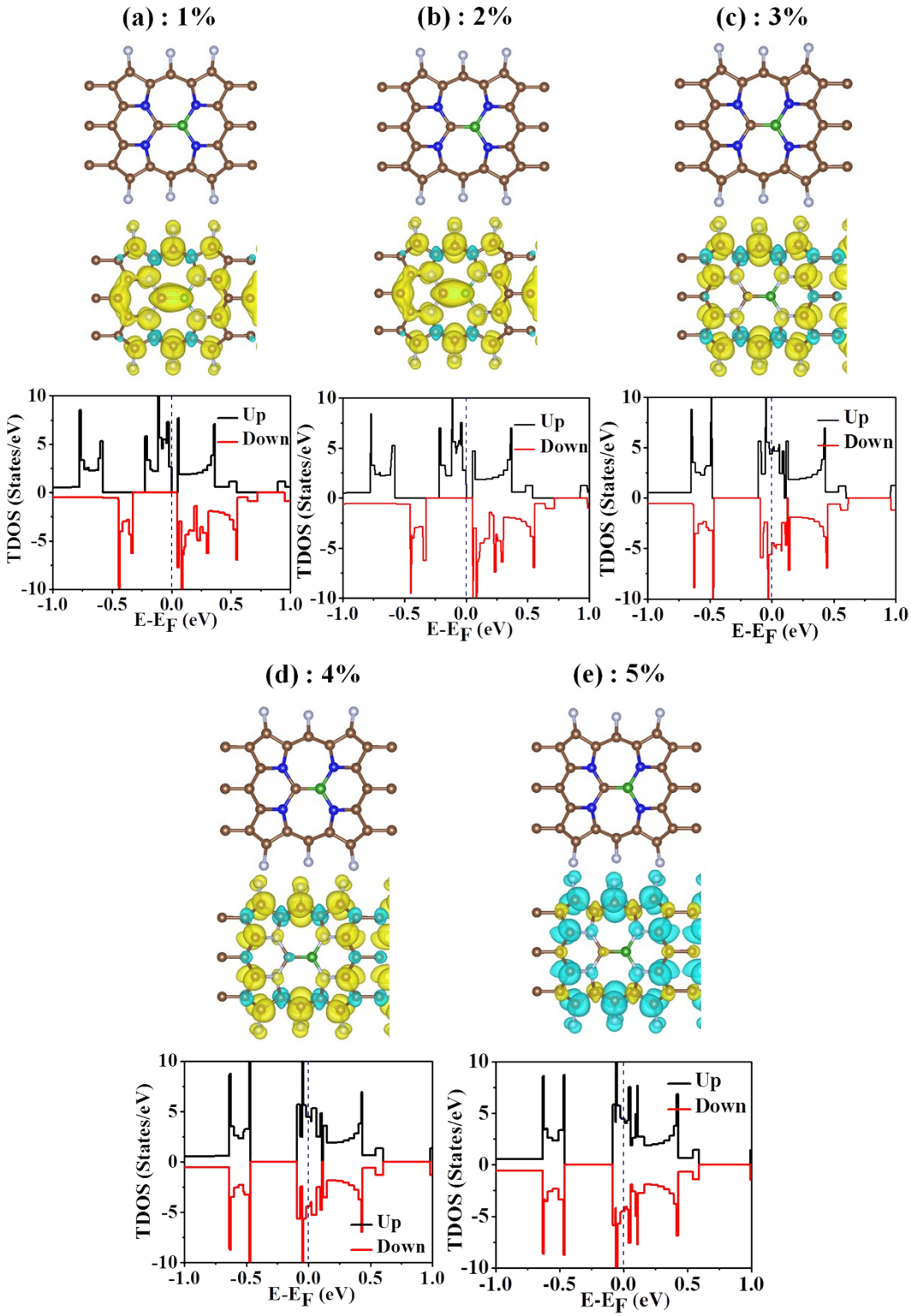
(a) : 1%
(b) : 2%
(c) : 3%
(d) : 4%
(e) : 5%
TDOS (States/eV)
E-E$_F$ (eV)
Up
Down

Figure S11: (a)-(e) Optimized structure, spin density distribution and TDOS plot of $B@(C=C)_a^F - PA$ under the application of uniaxial compressive strain from 1% to 5%.

Reference:

[1] G. Bhattacharyya, I. Choudhuri and B. Pathak, *Phys. Chem. Chem. Phys.* 2018, **20**, 22877-22889.

[2] H. Schöttke, *J. Less Common Met.* 1983, **91**, 159-165.

[3] W. Witt, *Z. Naturforsch. A*, 1967, **22A**, 92.

[4] I. Choudhuri, N. Patra, A. Mahata, R. Ahuja, B. Pathak, *J. Phys. Chem. C* 2015, **119**, 24827−24836.

[5] G. Bhattacharyya, I. Choudhuri, P. Bhauriyal, P. Garg, B. Pathak, *Nanoscale* 2018, **10**, 22280-22292.

[6] Y. Sun, Z. Zhuo, X. Wu and J. Yang, *Nano Lett.* 2017, **17**, 2771−2777.

[7] A. Schweiger and G. Jeschke, Principles of Pulse Electron Paramagnetic Resonance, Oxford University Press, Oxford, England, 2001.

[8] IUPAC Gold Book.

[9] S. Baroni, P. Giannozzi and A. Testa, Green's-function approach to linear response in solids. *Phys. Rev. Lett.* **1987**, 58, 1861-1864.

[10] A. Togo, F. Oba and I. Tanaka, *Phys. Rev. B: Condens. Matter Mater. Phys.* 2008, **78**, 134106-(1-9).

[11] S. Nose, *J. Chem. Phys.* 1984, **81**, 511-519.

[12] R. L. Kumawat, P. Garg, S. Kumar and B. Pathak, ACS *Appl. Mater. Interfaces* 2019, **11**, 219−225.

[13] M. Brandbyge, J. L. Mozos, P. Ordejón, J. Taylor and K. Stokbro, *Phys. Rev. B* 2002, **65**, 165401-(1-17).

[14] J. P. Perdew, K. Burke and M. Ernzerhof, *Phys. Rev. Lett.* 1996, **77**, 3865−3868.

[15] N. Troullier and J. L. Martins, *Phys. Rev. B* 1991, **43**, 1993-2006.

[16] A. R. Rocha, V. M. García-Suárez, S. Bailey, C. Lambert, J. Ferrer, S. Sanvito, *Phys. Rev. B* 2006, **73**, 085414-(1-22).

[17] B. He, J. Shen, D. Ma, Z. Lu, Z.Yang, *J. Phys. Chem. C* 2018, **122**, 20312−20322.

[18] S.-M. Jung, E. K. Lee, M. Choi, D. Shin, I.-Y. Jeon, J.-M. Seo, H. Y. Jeong, N. Park, J. H. Oh and J.-B. Baek, *Angew. Chem., Int. Ed.* 2014, **53**, 2398−2401.

[19] Y. A. Kim, K. Fujisawa, H. Muramatsu, T. Hayashi, M. Endo, T. Fujimori, K. Kaneko, M. Terrones, J. Behrends, A. Eckmann, C. Casiraghi, K. S. Novoselov, R. Saito, M. S. Dresselhaus, *ACS Nano*, 2012, **6**, 6293–6300.

[20] M. Endo, T. Hayashi, S.-H. Hong, T. Enoki, M. S. Dresselhaus, *J. Appl. Phys.* 2001, **90**, 5670-5674.

[21] S. Kawai, S. Saito, S. Osumi, S. Yamaguchi, A. S. Foster, P. Spijker and E. Meyer, *Nat. Comm.*, 2015, **6**, 8098.

[22] M. Xing, W. Fang, X. Yang, B. Tian and J. Zhang, *Chem. Commun.*, 2014, **50**, 6637-6640.

[23] T. P. Vaid, *J. Am. Chem. Soc.* 2011, **133**, 15838–15841.

[24] P. J. Brothers, *Chem. Commun.* 2008, **2008**, 2090–2102.

[25] G. Bhattacharyya, A. Mahata, I. Choudhuri and B. Pathak, *J. Phys. D Appl. Phys.* 2017, **50**, 405103.

[26] X. Wang, R. Wu, D. S. Wang and A. J. Freeman, *Phys. Rev. B: Condens. Matter Mater. Phys.* 1996, **54**, 61-64.

[27] J. Hu and R. Wu, *Phys. Rev. Lett.* 2013, **110**, 097202.

[28] D. S. Wang, R. Q. Wu and A. Freeman, *J. Phys. Rev. B: Condens. Matter Mater. Phys.* 1993, **47**, 14932.